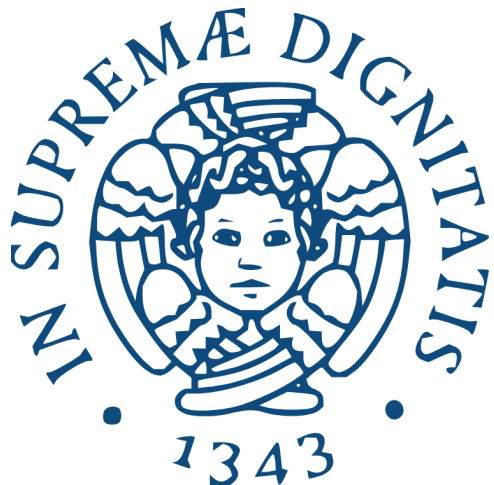


University of Pisa



Laboratory Report

# Analysis of the prompt emission from the Gamma-Ray Burst GRB130427A

## Professors:

Prof. Massimiliano Razzano  
Prof. Angelo Ricciardone  
Prof. Barbara Patricelli  
Prof. Andrea Pallottini

## Candidates:

Nicolò Aimone Braida (701844)  
Matilde Biscaro (702943)  
Lorenzo Nepi (701845)

## Abstract

The aim of this experience is to analyse the multiwavelength high-energy emission from Gamma-Ray Burst GRB130427A, which is an extremely energetic transient phenomena. The dataset has been collected by the detectors of the *Gamma-Ray Bursts Monitor* (GBM) onboard the NASA *Fermi* mission. The emission light curves were examined, and a spectral energy analysis was carried out. The results revealed the remarkably high energy and intensity emission of the phenomenon under investigation. Our dataset forced us to employ a T90 value provided by existing catalogues of  $(138.2 \pm 3.2)s$ . We used a Band function fit to analyse the spectral characteristics, obtaining a peak energy parameter of  $E_{peak} = 837 \pm 5keV$  and an isotropic energy of  $E_{iso} = 1.01^{+0.05}_{-0.03} \times 10^{54}erg$ . Thanks to the Hardness Ratio-T90 diagram, we could confirm that our GRB lives among the family of long GRBs. Finally, we verified that our target lies on the Amati relation.

## Contents

<b>1</b>	<b>Introduction</b>	<b>1</b>
1.1	Sources . . . . .	1
<b>2</b>	<b>GBM and LAT by <i>Fermi</i></b>	<b>2</b>
2.1	GBM . . . . .	2
<b>3</b>	<b>Target and Data</b>	<b>3</b>
<b>4</b>	<b>Data Analysis</b>	<b>3</b>
4.1	Light curve . . . . .	3
4.2	Spectral Analysis . . . . .	4
<b>5</b>	<b>Results</b>	<b>4</b>
<b>6</b>	<b>Discussion</b>	<b>8</b>
<b>7</b>	<b>Conclusion</b>	<b>9</b>
<b>8</b>	<b>Appendix</b>	<b>9</b>
8.1	Light Curve with Background . . . . .	9
8.2	Light Curve after subtracting Background	11
8.3	Light Curve thanks to GBM Data Tools employed in the Spectral Analysis . . . . .	13
8.4	Spectra thanks to GBM Data Tools employed in the Spectral Analysis . . . . .	14
<b>References</b>		<b>15</b>

## 1 Introduction

The development of X-ray astronomy is relatively recent. Unfortunately, X-rays are absorbed at altitudes of approximately 20–100 km in the Earth’s atmosphere by  $O_2$  and  $O_3$  molecules. For this reason, X-ray signals can only be observed from space. The first successful experiments are attributed to the group led by Rossi and Giacconi in 1962, who installed Geiger counters aboard an Aerobee

rocket [9]. Their goal was to measure the X-ray fluorescence emission from the lunar surface. However, instead of detecting lunar emission, they identified an intense x-ray radiation later associated with the source Scorpius X-1.

Still in the field of high energies, the development of gamma-ray astronomy has been significantly delayed due to several challenges. Once again, the opacity of the atmosphere at these wavelengths has made space-based observations essential. Moreover, the low fluxes and high background levels have required the use of highly advanced detectors.

In the 2000s, advances in the study of X-ray and  $\gamma$ -ray bands led to the identification of thousands of significant sources. Among these are GRBs (Gamma-Ray Bursts), that are extremely intense explosions of variable duration. Their isotropic distribution across the sky suggests an extragalactic origin. In support of this theory, some GRBs have been found to exhibit redshift values greater than  $z = 0.7$ .

### 1.1 Sources

Gamma-Ray Burst (GRB) sources are highly energetic relativistic phenomena. They are often described using the *Fireball model* (see Fig. 1), which involves a central engine, typically a black hole (BH) or a neutron star (NS), that powers the emission and triggers both internal and external shock processes:

- Internal shocks result from collisions between shells of matter moving at different velocities. These interactions account for the variability observed in the *prompt emission*;
- External shocks occur when the relativistic outflow interacts with the interstellar medium (ISM). Such interactions can lead to irregularities in the *afterglow*, especially when a shell encounters a region of enhanced density, such as a molecular cloud.

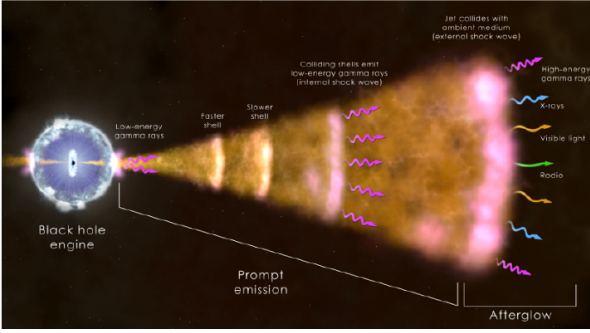


**Figure 1:** Representation of the fireball model.

The previously mentioned prompt emission (commonly referred to as a *flash*) has a variable duration ranging from a few milliseconds up to approximately 100 seconds. GRBs are classified into two main categories based on their prompt emission and on the parameter  $T_{90}$ , which is defined as the time interval during which the fluence increases from 5% to 95%, providing an estimate of the flash duration.

The first class comprehends *short GRBs*, with  $T_{90} < 2$  s, typically characterized by higher-energy photons. The second class, known as *long GRBs*, exhibits  $T_{90} > 2$  s. Each class is associated with a different progenitor:

- Short GRBs originate from the coalescence of compact object binaries, such as NS-NS or NS-BH systems;
- Long GRBs are caused by the collapse of massive stars, associated with core-collapse supernovae;
- Hybrid scenarios for events in between the two classes have also been proposed.

Following the prompt emission, GRBs exhibit a longer-lasting multiwavelength emission known as the afterglow, whose intensity typically decays following a power-law behaviour.

We define the *isotropic energy* as the energy irradiated assuming that the GRB emits uniformly in all directions.

$$E_{iso} = \frac{4\pi d_L^2}{(1+z)} S(E_1, E_2, z) \quad (1)$$

where  $d_L$  is the luminosity distance, and

$$S(E_1, E_2, z) = \int_{\epsilon_1}^{\epsilon_2} E N(E) dE,$$

where  $E_1, E_2$  are the maximum and minimum energy of the emission,  $\epsilon_1 = \frac{E_1}{(1+z)}$ ,  $\epsilon_2 = \frac{E_2}{(1+z)}$  and  $N(E)$  is the best fit model for the time-integrated spectrum. The luminosity distance  $d_L$ , according to the  $\Lambda$ CDM model, is given by

$$d_L = \frac{c}{H_0} (1+z) \int_0^{z_{ref}} \frac{1}{\sqrt{\Omega_m (1+z)^3 + \Omega_k (1+z)^2 + \Omega_\Lambda}} dz$$

with  $\Omega_k = 0$ ,  $\Omega_M = 0.3$  and  $\Omega_\Lambda = 0.7$ .

It is possible to establish an empirical relation between the isotropic energy  $E_{iso}$  and the peak energy  $E_{peak}$ . The latter is the energy corresponding to the maximum in the spectra which can be obtained from observational data and through spectral reconstruction (see Sec. 4.2). The

observed  $E_{peak}$  is corrected by multiplying it by  $(1+z)$  to account for the energy degradation due to cosmological redshift.

$$E_{peak} = E_{peak}^{obs} \times (1+z) \quad (2)$$

$E_{iso}$  and  $E_{peak}$  follow an empirical power-law relation known as the *Amati Relation* (see for example Fig. 16). Experimental observations have shown that long GRBs generally follow this trend, typically deviating by a few  $\sigma$ , while short GRBs tend to lie at systematically higher values.

## 2 GBM and LAT by *Fermi*

The following analysis is carried out using data from the Fermi mission.

Launched in 2008, NASA's *Fermi Gamma-ray Space Telescope* (formerly GLAST) is a space observatory designed to study the high-energy universe, particularly in the gamma-ray regime. One of its primary scientific goals is the observation and characterization of GRBs. Fermi carries two main instruments:

- The *Large Area Telescope* (LAT): sensitive to gamma rays from about 20 MeV to over 300 GeV, LAT provides wide-field coverage and enables the detection of high-energy GRB photons with excellent sensitivity and angular resolution;
- The *Gamma-ray Burst Monitor* (GBM): GBM covers a lower energy range (8 keV to 40 MeV) and is specifically designed to detect GRBs across the entire sky. It detects approximately 240 GRBs per year.

Fig. 2 represents the spectral coverage of the GLAST.

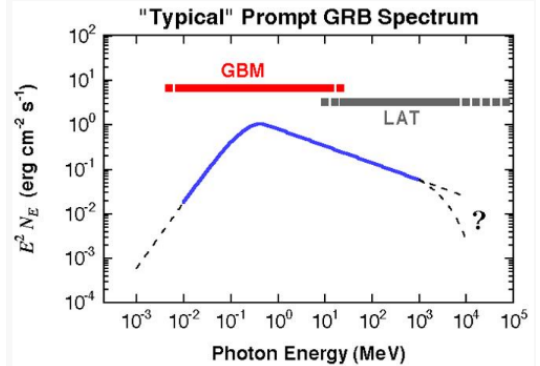


**Figure 2:** Spectral coverage of GBM and the LAT compared with a typical GRB spectrum [2]

If GBM detects a GRB above a fixed threshold, *Fermi* automatically slews to move the GRB into LAT field of view (FOV). GBM provides precise GRB locations over a wide FOV that can be used to repoint the LAT at particularly interesting bursts (both inside and outside the LAT FOV) for gamma-ray afterglow observations. The joint analysis of data from both GBM and LAT offers a robust mean to investigate GRB spectra and the fundamental physical processes driving them.

### 2.1 GBM

Let us analyse some GBM features. The detector capabilities are summarized in Tab. 1. GBM employs two

**Table 1:** GBM detector specifics [2].

Parameter	Value
Low Energy Limit	<10keV
High Energy Limit	>25MeV
Energy Resolution (FWHM, 0.1-1MeV)	<10%
Field of View (Co-aligned with LAT FOV)	>8sr
Time Accuracy (Relative to spacecraft time)	<10 microseconds
Average Dead Time	<10 microseconds/count
Burst Sensitivity (Peak 50-300 keV flux for $5\sigma$ detection in $\text{ph cm}^{-2} \text{s}^{-1}$ )	<0.5cm $^{-2}$
Burst Alert Locations (1 $\sigma$ systematic error radius)	<15°
Burst Alert Time Delay (Time from burst trigger to spacecraft notification, used to notify ground of LAT)	<2s

different types of cylindrical crystal scintillation detectors and the collected light is read out by photomultiplier tubes (PMTs). The lower end of the energy range (8 keV-1 MeV) is covered by an array of 12 sodium iodide (NaI) detectors, distributed around the Fermi spacecraft with several orientations to provide the required sensitivity and FOV. To also cover higher energies (150 keV-30 MeV), the GBM includes two bismuth germanate (BGO) detectors. This material is characterized by high density ( $7.1 \text{ gcm}^{-3}$ ) and large effective atomic number ( $Z \sim 63$ ). These features allow GBM to detect photons beyond the low energy end of the LAT at  $\sim 20$  MeV. The BGO detectors are mounted on opposite sides of the Fermi spacecraft, providing high-energy spectral coverage over approximately the same field of view as the NaI detectors. The *Data Processing Unit* (DPU) collects signals from all 14 GBM detectors. It digitalizes and time-tags the pulse height signals from the detectors, and packages the resulting data into several formats for transmission to the ground. Fig. 3 shows 3D models of the GBM detectors.

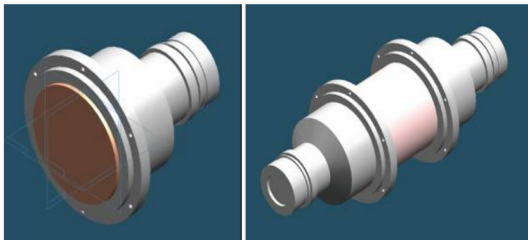


**Figure 3:** The Fermi GBM's NaI (on the left) and BGO (on the right) detectors [2].

### 3 Target and Data

According to [6], at 07:47:06.42 UT on 27 April 2013, the Fermi Gamma-Ray Burst Monitor triggered and located GRB 130427A, which was also detected by Swift/BAT and Fermi/LAT. The GBM on-ground location ( $\alpha, \delta$ ) = ( $173^\circ, 27.2^\circ$ ) is consistent with the Swift position. The Swift detectors 6, 9, 10 had been triggered. GRB 130427A is an extremely energetic and well-known long GRB (see [8]). In this report we are going to investigate some features of its prompt emission using data from the Fermi-GBM Burst catalogue [4].

After constructing the light curve of each detector of GBM to investigate which one was triggered by the signal, we will proceed to perform a time-domain analysis of the GRB prompt emission, determining the parameters of interest such as the background level and the  $T_{90}$  value. In

the second part, we will perform spectral analysis of the emission using GBM data tools [3]. The collected data consist of several lists of photons, each associated with its arrival time and energy channel (*Time-Tagged Event* data, TTE). Both the actual GRB emission and the detected background contribute to the observed count for each channel. TTE data are stored in .fits file, one for each detector.

## 4 Data Analysis

### 4.1 Light curve

First of all, we selected TTE files, related to the NaI detectors and the two BGO detectors. Then, we plotted the count-per-time bin light curve (see App. 8.1) for each detector assuming the GBM time resolution of 1.024 s as a good candidate for the width of the bins. To estimate the background, we roughly selected a time interval which excluded the transient event and estimated the mean and standard deviation of the remaining counts (Tab. 2). Since their value were reasonably stable, we fitted them with their mean and subtracted the background contribution in the light curve of each detector (see App. 8.2). In this case, it is important to note that the tail of our GRBs does not exhibit a purely exponential decay; instead, the emission appears to continue, leading to a small peak in the light curve following the prompt emission. This late signal can not be considered neither as background, nor as afterglow phenomena, because it happens a few minutes after the prompt (afterglow flares have timescales of days, or even months). It was then treated as part of the emission. In Sec. 5 we will provide a more detailed justification of this choice and analyse how this secondary prompt will affect our  $T_{90}$  estimate.

At this point it is possible to establish which detector was triggered by the event by setting a threshold of  $5\sigma$  over the mean of the background counts for the prompt counts (*Background Trigger Selection*, BTS). We carried on by computing  $T_{90}$  value to estimate the duration of the burst by subtracting  $T_5$  from  $T_{95}$ . These are defined as the timestamps at which 5% and 95% of the total photons from the burst have been detected, respectively. The  $T_{90}$  value can be calculated either separately for NaI and BGO or by combining data from all detectors, since it characterizes the GRB itself. The number of counts in the tail collected by GBM detectors weren't enough to reach an accurate estimation of our  $T_{90}$ , so we chose the value provided by [6].

## 4.2 Spectral Analysis

In order to perform spectral analysis, it is necessary to choose a model spectrum that can be described in terms of a few parameters and infer such parameters through a fit on the data. For each model, a predicted spectrum is computed and compared with the observed data. Using our dataset and the **GBM Data Tools**, we took into account the observed count spectrum, the instrumental response and the model spectrum.

The spectrum is typically non-thermal and is phenomenologically described by a *Band function*  $f(E)$ :

$$f(E) = \begin{cases} A \left( \frac{E}{100 \text{ keV}} \right)^\alpha \exp \left( -\frac{(\alpha+2)E}{E_{peak}} \right) & \text{for } E < (\alpha - \beta) \cdot \frac{E_{peak}}{\alpha+2} \\ A \left( \frac{E}{100 \text{ keV}} \right)^\beta \exp(\beta - \alpha) \left( \frac{(\alpha-\beta)E_{peak}}{100 \text{ keV} \cdot (\alpha+2)} \right)^{\alpha-\beta} & \text{otherwise} \end{cases} \quad (3)$$

For afterglow emission a Power Law model is commonly used.

It is necessary to perform a best-fit of the Band model to the NaI and GBO data. First of all, we performed light-curve fitting and background estimation thanks to the `gbm.data` tools, and also plotted the spectra. For each detector we chose an effective energy range (100-1000 keV for NaI and 150-30000 keV for BGO). Even if the BTS method applied to our data suggested that all the instruments were triggered, we selected only NaI detectors number 6,9, and 10 according to [6].

Then we proceeded by fitting the energy spectra with a function obtained by the superposition of several components: Band, Comptonized, Black Body, and Power Law functions. The best-fitting function is then selected based on the *PGstat/DoF* value, a parameter that quantifies the goodness of fit<sup>1</sup>. However such parameter resulted unusable for our spectra (see Sec. 5), so we simply employed a single Band function as the best phenomenological description.

We proceeded by computing the flux in the 10-50 keV range (channel 2), and in the 50-300 keV range (channel 3), and determining the so called spectral *Hardness ratio* defined as

$$\text{HR}_{32} = \frac{\text{Fluence}_{\text{channel}3}}{\text{Fluence}_{\text{channel}2}}. \quad (4)$$

Now we could estimate the  $E_{peak}$  and subsequently  $E_{iso}$  through Eq. 1. We use a redshift equal to  $z = 0.34$  as reported in [8]. Finally, it was possible to verify where our GRB set in the Amati relation [1] (Fig. 16).

## 5 Results

According to [8], the light curve revealed by Swift-BAT in the 15-150 keV band, can be divided in three parts: an initial emission, which begins at  $t = 0.1$  s and peaks at  $t = 0.5$  s; a second large peaks, showing a complex composition with a duration of 20 s; and a third much weaker episode, starting around  $t = 120$  s and showing a fast-rise/exponential decay behaviour. Looking at our GRB-light curve features, it results pretty hard to recognize the third component (see App. 8.1), while it is clearly visible in light curves measured by Swift BAT, as the one presented in Fig. 1 of [8]. For the following discussion we are going to take the detector NaI6 as an example, but all of our detectors were triggered by the event (see Sec.

8). During the manual background estimation, although the third peak was not clearly visible, we excluded a time window from approximately 110 to 300 s. This choice allowed us to treat the third peak as part of the signal and to compute the background as the mean count rate outside this interval, as previously explained. An example of the light curve before and after background subtraction is shown in Fig. 4 while the different values and the relative standard deviation for all the detectors are listed in Tab. 2.

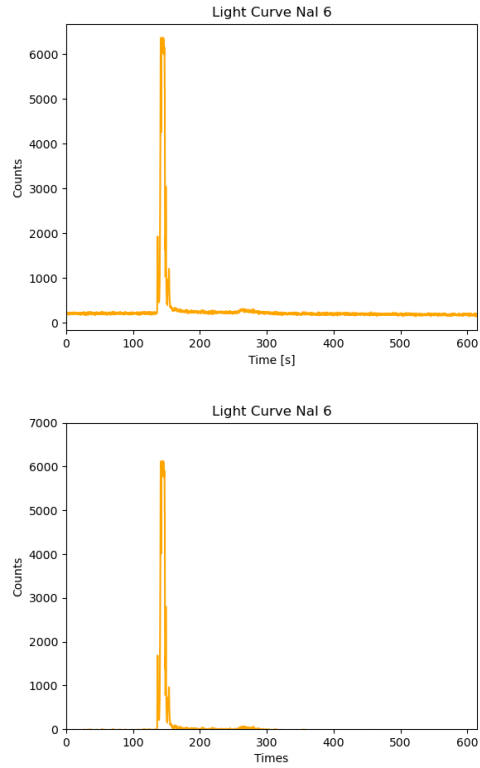


**Figure 4:** Light Curve detected by NaI6 detector before background subtraction (left) and after (right).

**Table 2:** Background average counts and standard deviation for each detector.

Detector	Average (counts)	StD. (counts)
NaI0	196	17
NaI1	173	16
NaI2	275	27
NaI3	217	23
NaI4	214	19
NaI5	270	21
NaI6	245	16
NaI7	280	18
NaI8	234	37
NaI9	255	43
NaI10	209	17
NaI11	245	18
BGO0	337	22
BGO1	417	24

After background subtraction, the  $T_{90}$  value was computed as described in Sec. 4. Initially, the analysis was performed separately for the two types of detectors, but we subsequently adopted the mean and standard deviation (as its uncertainty) calculated over the combined set of all  $T_{90}$  values. The computed values are shown in Tab. 3.

<sup>1</sup>More precisely, PGstat is a Poissonian count statistic with Gaussian Background and DoF stands for "degrees of freedom".

**Table 3:**  $T_{90}$  and standard deviation calculated in absolute time.

Parameter	Average (s)	StD. (s)
$T_5$	138.5	1.4
$T_{95}$	148.2	6.6
$T_{90}$	9.7	5.7

This result is not consistent with the  $T_{90}$  value provided by the Fermi-Catalogue [2].

For the spectral-fitting part we had three options: on one hand we could have employed the  $T_{90}$  value given by [4] and [6], that is  $(138.2 \pm 3.2)$  s; on the other hand we could have tried to find the best fit in an interval from  $T_0 + 0.002$  s<sup>2</sup> and  $T_0 + 18.42$  s, according to the informations provided by [5]; finally, we could have used our independently found value. In [5], it is stated that, due to the intense brightness of the burst, systematic uncertainties become significant, and no individual model achieves a satisfactory fit in this initial analysis.

All three possibilities were explored to assess whether any could yield a more reliable result.

From this point one our analysis was carried out using to the **GBM Data Tools**.

To proceed with the spectral analysis, we repeated background subtraction using the **GBM Data Tools** (Fig. 5). We also generated the energy spectra by applying the effective energy limits for each instrument as shown in Fig. 6. Due to software constraints (specifically the **GBM Data Tools** limitation to a maximum of 12 detectors), we had to exclude the last two NaI units from the analysis.

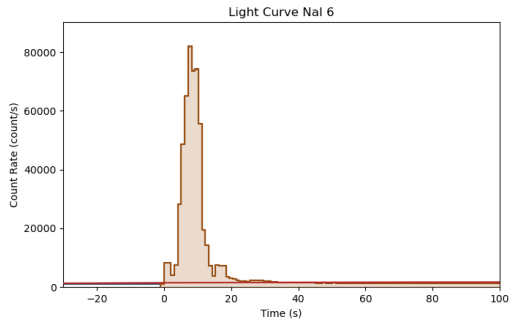


**Figure 5:** Light Curve detected by NaI6 detector analysed by GBM Data Tools

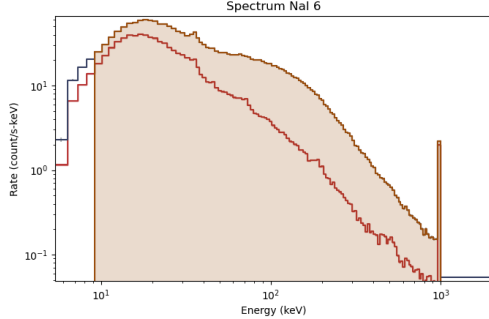


**Figure 6:** Energy-spectrum by NaI6 detector analysed by GBM Data Tools

First of all, we tried a band-function-fit employing the  $T_{90}$  value provided by the Fermi-Catalog (138 s). The fitted parameters are presented in Tab. 4. Consider that

<sup>2</sup> $T_0$  is defined as the time where the emission is first detected.

$E_{pivot}$  has a fixed instrumental value of approximately 100 keV.

**Table 4:** Fitted parameters computed for a searching range of  $T_0 - T_0 + 138$  s.

Par.	Value	Error <sup>+</sup>	Error <sup>-</sup>
$A$ (ph/s/cm <sup>2</sup> /keV)	$3.4 \times 10^{-2}$	$7.6 \times 10^{-5}$	$9.4 \times 10^{-5}$
$E_{peak}$ (keV)	$2.1 \times 10^4$	$1.3 \times 10^2$	$1.3 \times 10^2$
$\alpha$	$-8.8 \times 10^{-1}$	$9.4 \times 10^{-4}$	$1.1 \times 10^{-3}$
$\beta$	-8.2	1.8	5.2
Pgstat/DoF	1408139/1455		

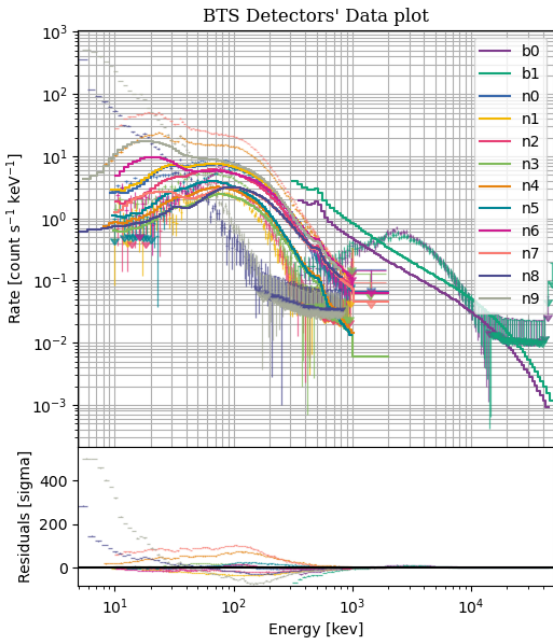


**Figure 7:** Fitted Band functions (above) and residuals (below) for a searching range of  $T_0 - T_0 + 138$  s.

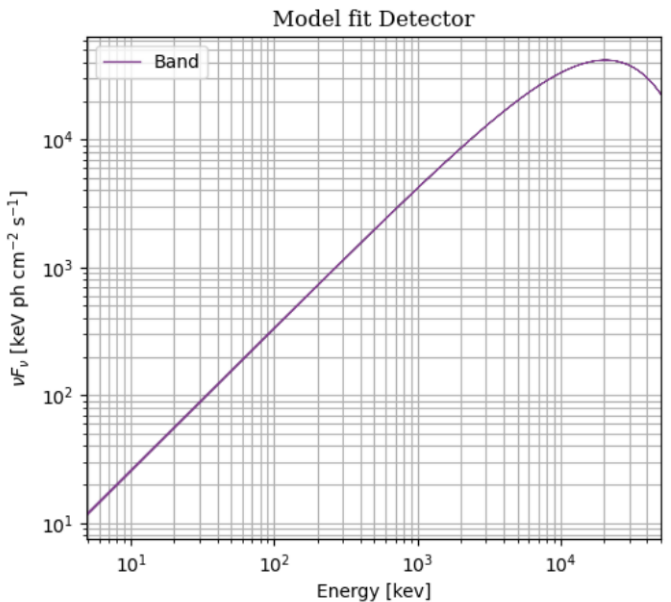


**Figure 8:** Best model fit obtained with a Band function and a searching range of  $T_0 - T_0 + 138$  s.

Fig. 9, 10 and Tab. 5 show the results for the spectral fit for the time-interval provided by [5].

**Table 5:** Values provided by a searching range of  $T_0+0.002$  s -  $T_0+18.432$  s.

Par.	Value	Error <sup>+</sup>	Error <sup>-</sup>
$A$ (ph/s/cm <sup>2</sup> /keV)	$4.4 \times 10^{-1}$	$8.0 \times 10^{-4}$	$7.6 \times 10^{-4}$
$E_{peak}$ (keV)	$9.9 \times 10^4$	$5.1 \times 10^4$	$1.5 \times 10^2$
$\alpha$	-1.3	$8.2 \times 10^{-4}$	$6.7 \times 10^{-4}$
$\beta$	-2.0	0.0	$2.4 \times 10^{-3}$
Pgstat/DoF	2526191.01/1455		

**Table 6:** Values provided by a searching range of  $T_0-T_0+9.67$  s.

Par.	Value	Error <sup>+</sup>	Error <sup>-</sup>
$A$ (ph/s/cm <sup>2</sup> /keV)	$6.3 \times 10^{-1}$	$1.0 \times 10^{-3}$	$1.5 \times 10^{-3}$
$E_{peak}$ (keV)	$3.5 \times 10^5$	$1.5 \times 10^6$	$1.6 \times 10^3$
$\alpha$	-1.2	$7.3 \times 10^{-4}$	$7.9 \times 10^{-4}$
$\beta$	-2.0	0.0	8.0
Pgstat/DoF	2074678/1455		

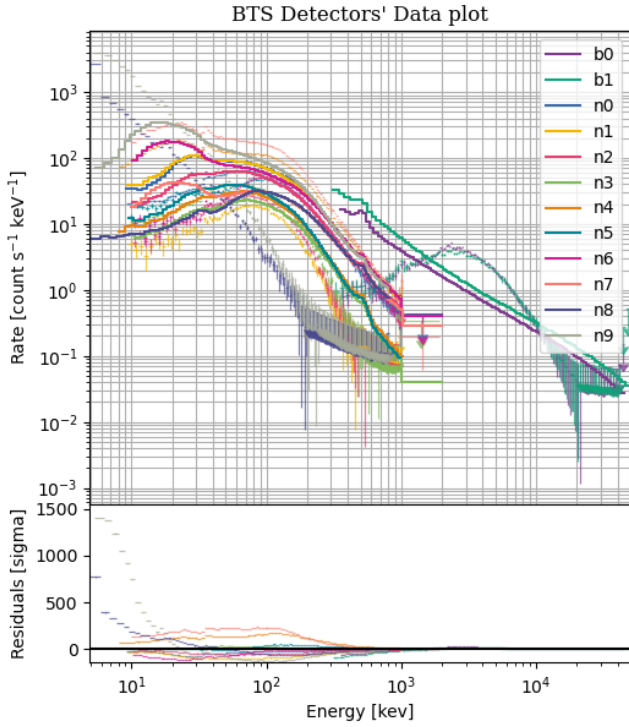


**Figure 9:** Fitted Band functions (*above*) and residuals (*below*) for a searching range of  $T_0+0.002$  s -  $T_0+18.432$  s.

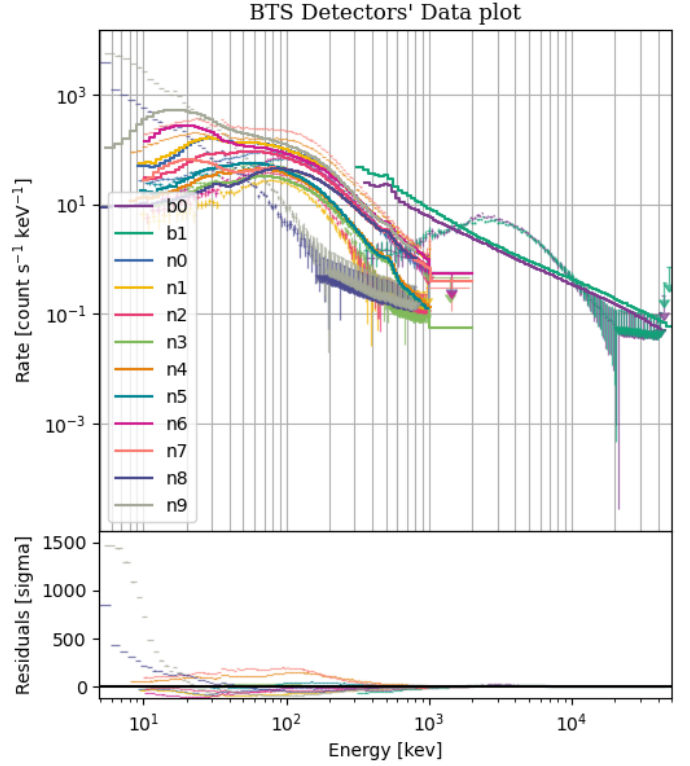


**Figure 11:** Fitted Band functions (*above*) and residuals (*below*) for a searching range of  $T_0-T_0+9.67$  s.

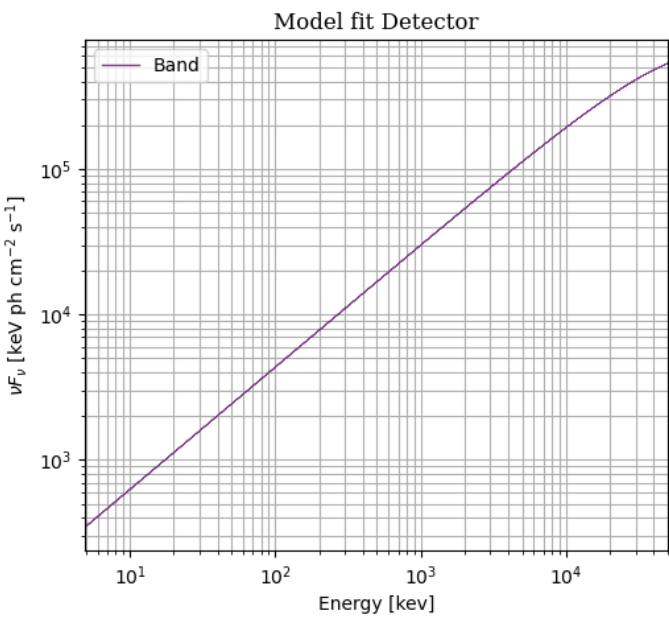


**Figure 10:** Best model fit obtained with a Band function and a searching range of  $T_0+0.002$  s -  $T_0+18.432$  s.

Ultimately, we made an attempt employing the  $T_{90}$  calculated above (Fig. 11, Fig. 12 and Tab. 6)

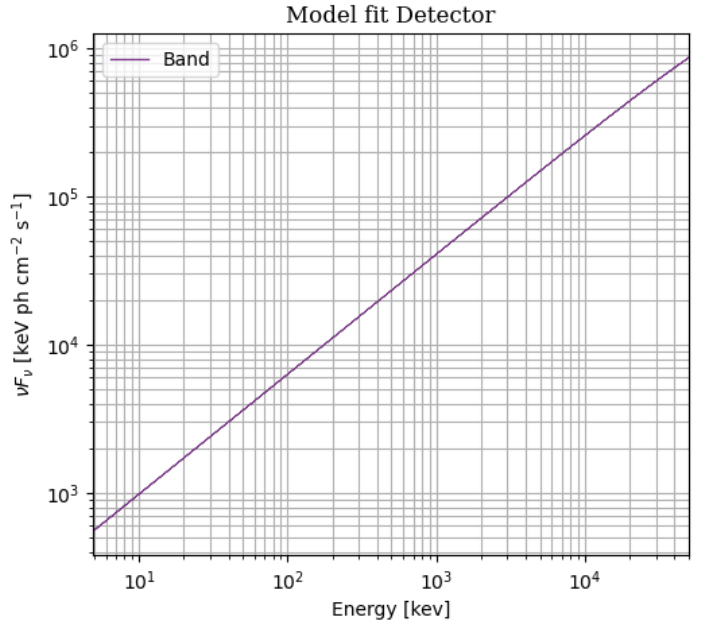


**Figure 12:** Best fit model fit obtained with a Band function and a searching range of  $T_0-T_0+9.67$  s.

Considering that the value of Pgstat/DoF should be around 1 to achieve a good fit, we can state that this kind of statistic is unsuitable for our emission. The best  $T_{90}$  we

can use is the one provided by [4]. We also tried several compositions for our fitting function searching for a better Pgstat/Dof, without success. The attempts for a better fitting functions and the resulting PGstat/DoF values are summarized in Tab. 7.

**Table 7:** Comparison of PGstat/DoF for different spectral models.

Model	Pgstat/DoF
Band + Power Law	1423663 / 1453
Power Law	1423664 / 1457
Band + Comptonized	1408140 / 1452
Band + Blackbody	1270181 / 1453

The fact that the Pgstat/DoF consistently remains of the same order of magnitude—nearly three orders of magnitude higher than expected—suggests the presence of a systematic error in the underlying assumptions.

Knowing this, we decided to ignore our rough calculation of BTS and select only the detectors that had been triggered according to [6]. They are NaI detectors number 6, 9 and 10 (see App. 8 for light curves and spectra frames). So we repeated our analysis and the best fit we reached was still thanks to a Band function. The resulting parameters are exposed in the Tab. 8.

**Table 8:** Band model parameters fitted over the selected interval. Epiv fixed at 100 keV.

Par.	Value	Error <sup>+</sup>	Error <sup>-</sup>
A (ph/s/cm <sup>2</sup> /keV)	$1.2 \times 10^{-1}$	$3.2 \times 10^{-4}$	$3.1 \times 10^{-4}$
E <sub>peak</sub> (keV)	$8.4 \times 10^2$	5.0	4.9
$\alpha$	$-7.5 \times 10^{-1}$	$3.6 \times 10^{-3}$	$3.6 \times 10^{-3}$
$\beta$	-2.5	$1.2 \times 10^{-1}$	$9.3 \times 10^{-2}$
Pgstat/DoF	3450 / 362		

Although the new value for the PGstat/DoF is not yet statistically significant, it is at least of the expected order of magnitude. The fit is certainly improved, although still not completely satisfactory.

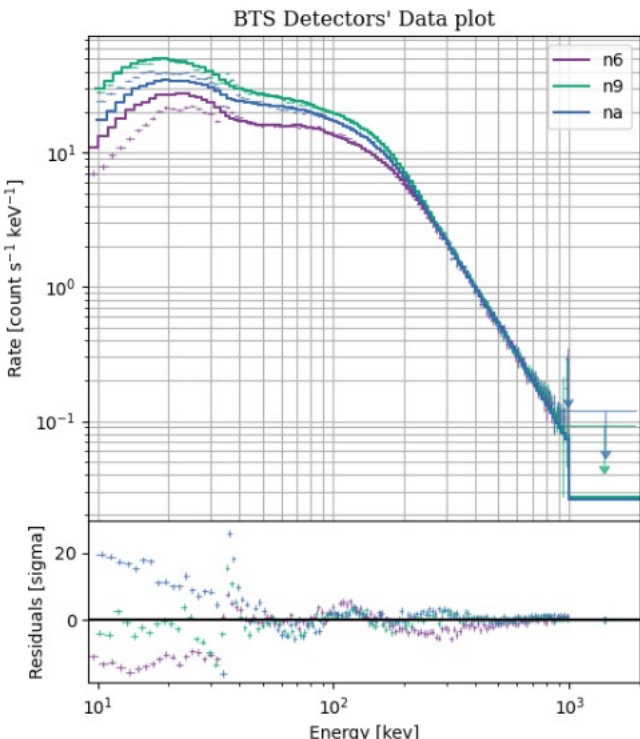


**Figure 13:** Fitted Band functions (above) and residuals (below) with detectors NaI6 NaI9 NaI10 and a searching range of  $T_0-T_0+138s$ .

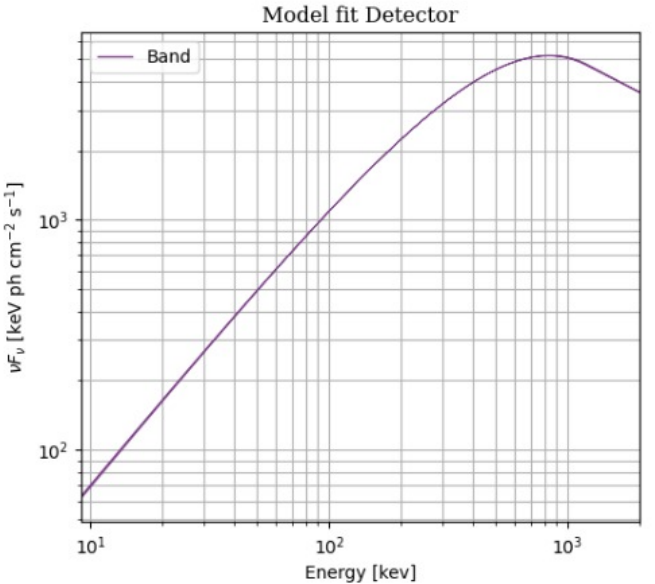


**Figure 14:** Best fit model with detectors NaI6 NaI9 NaI10 and a searching range of  $T_0-T_0+138s$

We then evaluated

$$E_{\text{peak}} = 837 \pm 5 \text{ keV}.$$

This result is coherent with the catalogue [5]. Since we have not taken instrumental errors into account, our uncertainty may be underestimated. To find the Hardness ratio, we calculated the fluence in the energy channels 2 (10-50 keV) and 3 (50-300 keV) (Tab. 9).

**Table 9:** Energy Flux in channels 2 and 3.

Channel	Energy FLux (erg/s/cm <sup>2</sup> )	Error (erg/s/cm <sup>2</sup> )
2	$5.617 \times 10^{-7}$	$1.0 \times 10^{-9}$
3	$4.376 \times 10^{-6}$	$2.2 \times 10^{-8}$

Referring to the Eq. 4 and considering

$$\text{Fluence} \approx \text{Flux} \cdot T_{90}, \quad (5)$$

it can be noted that the Hardness ratio does not depend on the  $T_{90}$  value; therefore to estimate  $HR_{32}$ , it is sufficient to compute the ratio between the energy flux values and propagate the associated errors. We chose to use the maximum error on the fluxes of the two channels. Since the uncertainties on the parameters (automatically computed by GBM Data Tools) are asymmetric, we calculated the maximum and minimum possible values of the flux and symmetrized the error by selecting the largest deviation from the central value. Despite this rather rough estimate, the resulting uncertainty still appears to be significantly underestimated. In the end, the Hardness ratio value we estimated is

$$HR_{32} = 7.791 \pm 0.003.$$

We then plotted our GRB data in the Hardness Ratio -  $T_{90}$  plot taken from [7] (Fig. 15). We could not find our GRB in this plot, but we are not sure if our target was taken into account in this catalogue. However, it surely belongs to the long GRBs group. Subsequently,

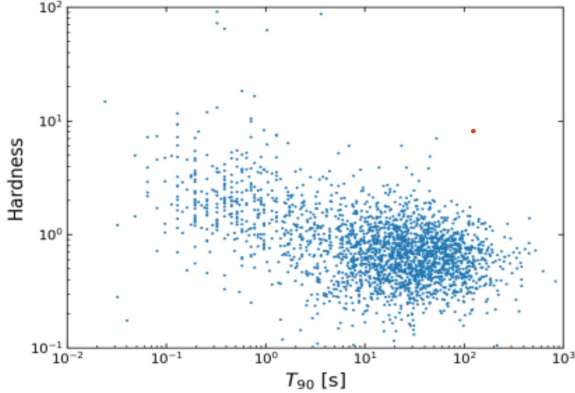


**Figure 15:** Hardness Ratio -  $T_{90}$  plot by [7]. The red dot represents GRB130427A.

we multiplied the peak energy obtained from the fit by a correction factor due to the redshift,  $(1+z)$ , obtaining

$$E_{\text{peak}} = E_{\text{peak}}^{\text{obs}}(1+z) = 1122.5^{+6.7}_{-6.5} \text{ keV}.$$

This result is approximately coherent with the model shown in Fig. 8, but not compatible with the value in [8]. Once again, it is clear that our uncertainty is likely underestimated.

We proceed by computing the luminosity distance:

$$d_L = 5.71 \times 10^{27} \text{ cm} .$$

Moreover, since we knew that  $z = 0.34$ , we were able to compute  $E_{\text{iso}}$ :

$$E_{\text{iso}} = 1.01^{+0.05}_{-0.03} \times 10^{54} \text{ erg}.$$

This value seems reasonable, but is not consistent within the uncertainty range with the result reported in the literature. Once again, this suggests that our uncertainty is likely underestimated due to systematic errors.

Finally, we proceeded by plotting the Amati Relations, thanks to the parameters provided by [1]. Our GRB was found to lie remarkably close to the Amati relation line, despite the presence of an underestimated error.

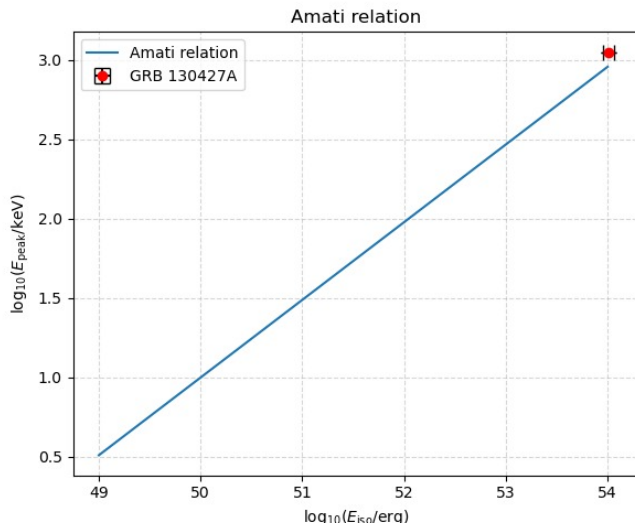


**Figure 16:** GRB130427 on the Amati relation.

## 6 Discussion

First of all, we are confident to state, thanks to the comparison with [6], that our method for evaluating the triggered detectors by applying a threshold of  $5\sigma$  was very approximate. The reality of facts shows that only NaI6, NaI9, and NaI10 were actually triggered.

Thanks to information available in the literature, we understood that GRB 130427A is the most energetic burst ever detected by the GBM and directed our analysis accordingly. However, the GBM instruments proved to be not particularly well suited for our specific study.

Firstly, we were unable to clearly distinguish the full duration of the burst above the background level. As a result, our value of the  $T_{90}$  duration is significantly underestimated and should be interpreted with caution.

Therefore, we decided to fall back on the  $T_{90}$  found in the catalogues, choosing the one from [4] as the best candidate. Nevertheless, it proved unsuitable when used as the searching-range parameter during spectral fitting, as the PGstat/DoF value was systematically very high.

By considering only the detectors that were actually triggered, the Band function proves to be the best description for fitting our event. In terms of PGstat/DoF, we still obtain a value far from 1, but of the same order of magnitude, and therefore certainly more reasonable.

This fit also returns values for the parameters  $A$ ,  $E_{\text{peak}}$ ,  $\alpha$ , and  $\beta$  that are consistent with those reported in various catalogues, such as [4, 6, 8]. A possible reason for the high PGstat/DoF values could be the underestimation of the uncertainties associated with the data. In the case of very bright bursts, Poisson noise may not fully account for the total uncertainty; systematic errors, such as those arising from the instrument response to such an energetic signal, might not have been adequately considered.

The value of  $E_{\text{iso}}$  turned out to be reasonable, but slightly overestimated, and this is reflected in the position of our GRB with respect to the Amati relation line.

The location of our GRB in the Hardness ratio -  $T_{90}$  diagram provided a confirmation that our GRB is classified among the long-duration bursts.

It is also important to investigate the correspondence between the redshift and the energy of this GRB, based on the referenced article [8] and the results we have obtained. In the nearby Universe ( $z < 0.4$ ), only a few long-duration GRBs have been detected. These events typically exhibit relatively low isotropic energies ( $E_{\text{iso}} \lesssim 10^{52}$  erg) and are associated with type Ib/c supernovae (often classified as hypernovae due to their broad spectral lines and high expansion velocities).

GRB 130427A, however, stands out as an exceptionally powerful event, more similar to those commonly observed at high redshift ( $z > 1$ , with an average of  $z \sim 2$ ). Its proximity provides a rare opportunity to investigate whether such high-luminosity GRBs share the same characteristics as their distant counterparts, and whether they are accompanied by supernovae.

The detection of SN 2013cq, associated with this burst, confirms that even highly energetic GRBs can be linked to supernovae, a connection previously observed only for weaker nearby bursts. While one might expect that most of the energy in powerful GRBs is consumed by the relativistic jet, leaving little space for a supernova explosion,

GRB 130427A clearly demonstrates that this is not necessarily the case [8].

## 7 Conclusion

In conclusion, GRB 130427A represents a rather exceptional event. Its long duration and high released energy posed several challenges during the analysis. Fortunately, where our results proved insufficient, we were able to rely on data available from various catalogues to proceed with the spectral analysis. Ultimately, our study focused on the prompt emission of the event, without taking into account potential afterglow phases. As a result, any hypothesis regarding the origin and nature of the GRB remains highly uncertain.

## 8 Appendix

### 8.1 Light Curve with Background

Fig. 17-30 show the measured light curves.

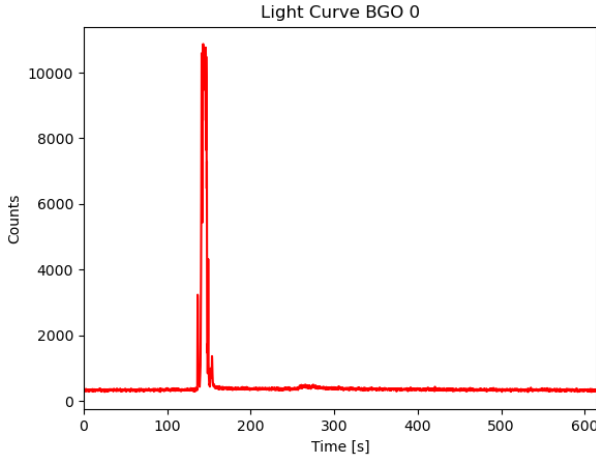


**Figure 17:** Light Curve detected by BG00 detector.

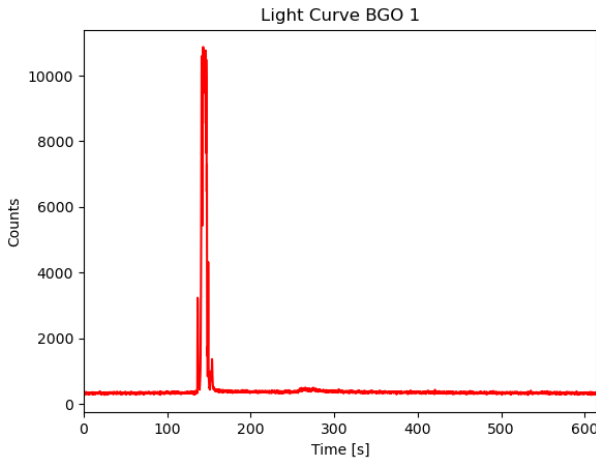


**Figure 18:** Light Curve detected by BGO1 detector.

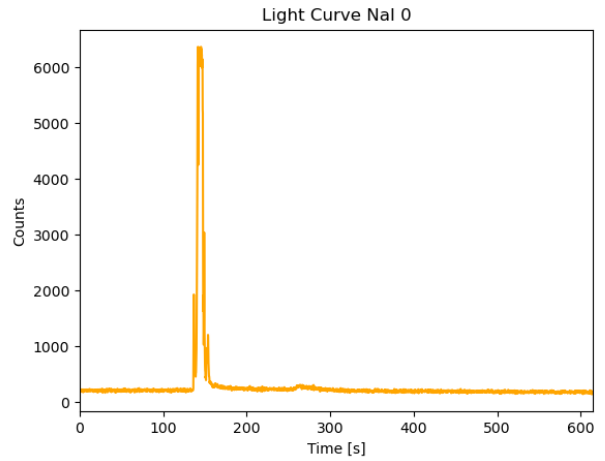


**Figure 19:** Light Curve detected by NaI0 detector.

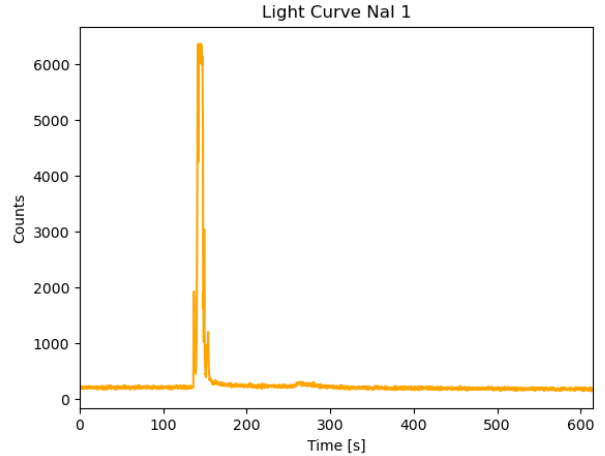


**Figure 20:** Light Curve detected by NaI1 detector.

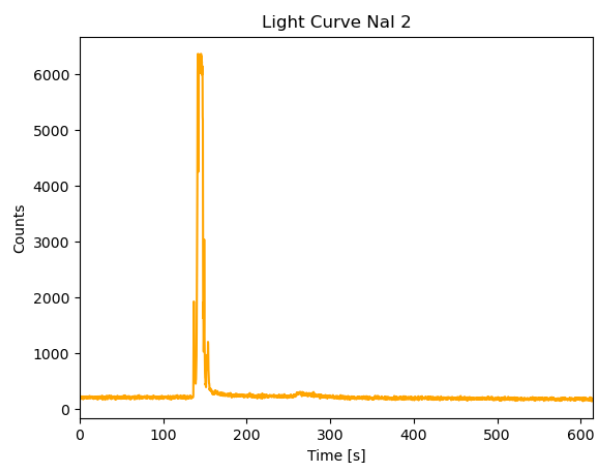


**Figure 21:** Light Curve detected by NaI2 detector.

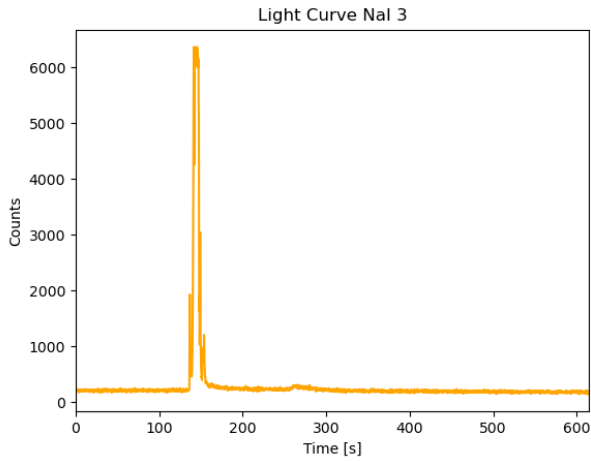


**Figure 22:** Light Curve detected by NaI3 detector.

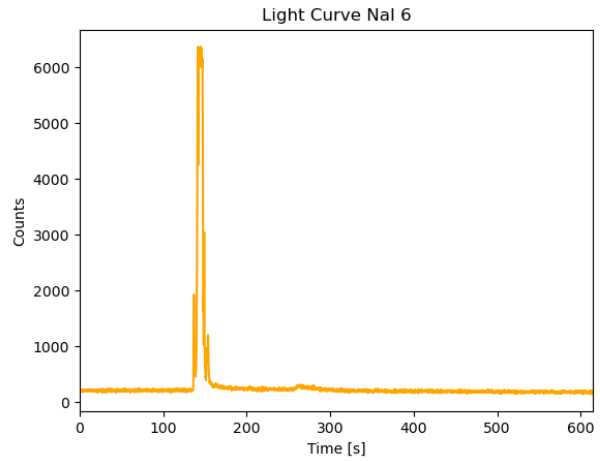


**Figure 25:** Light Curve detected by NaI6 detector.

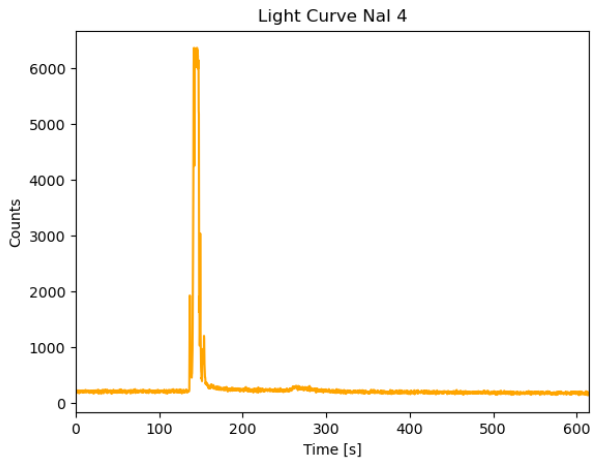


**Figure 23:** Light Curve detected by NaI4 detector.

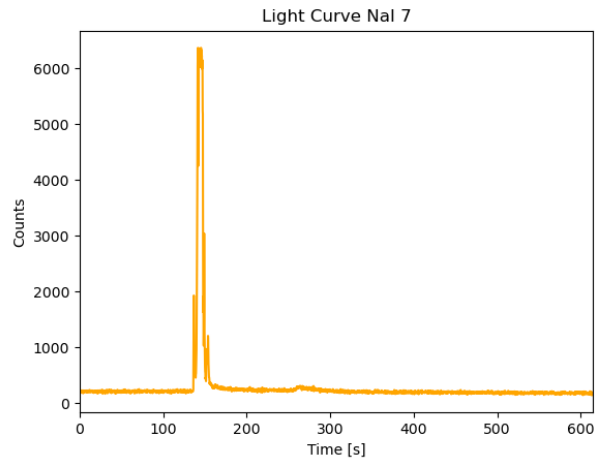


**Figure 26:** Light Curve detected by NaI7 detector.

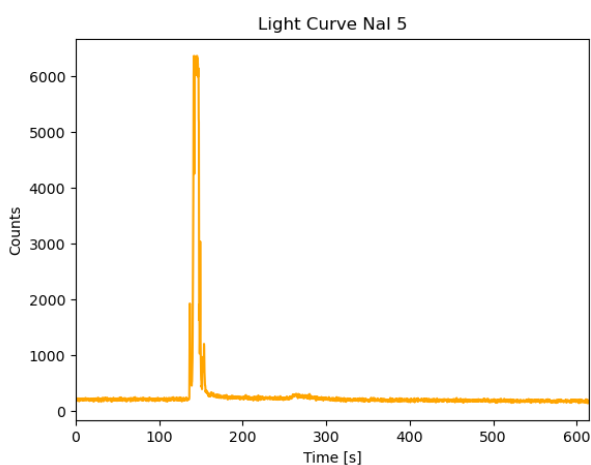


**Figure 24:** Light Curve detected by NaI5 detector.

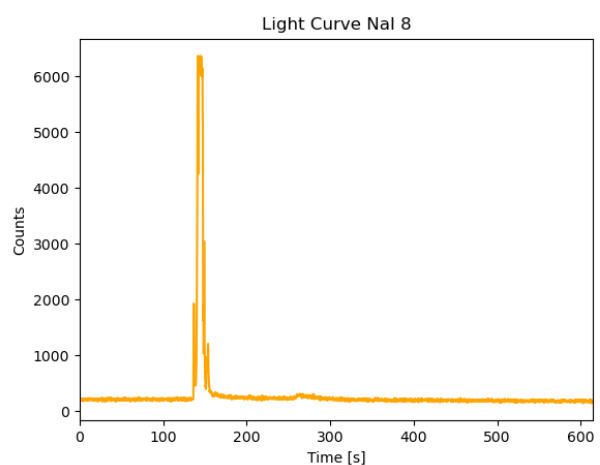


**Figure 27:** Light Curve detected by NaI8 detector.

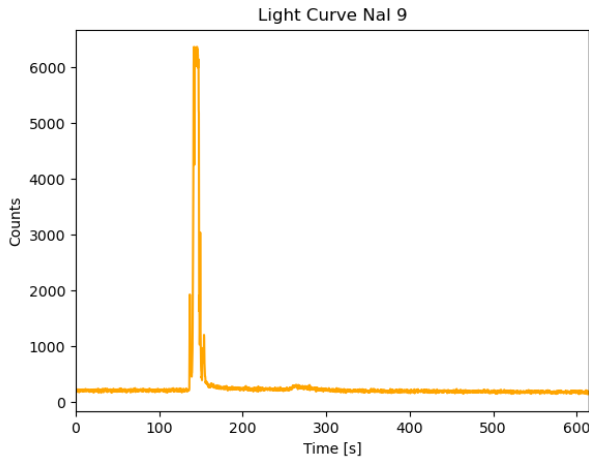


**Figure 28:** Light Curve detected by NaI9 detector.

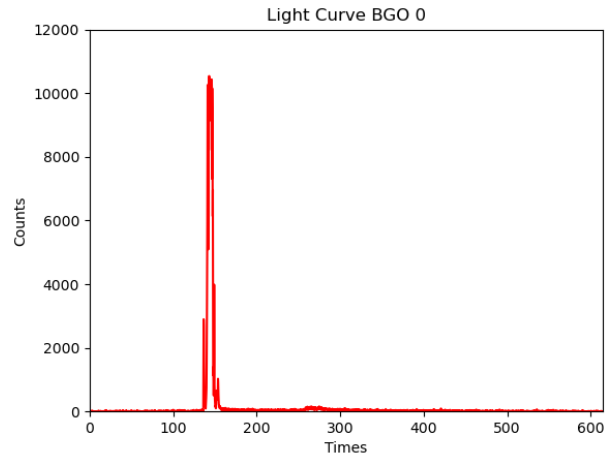


**Figure 31:** Light Curve detected by BGO0 detector.

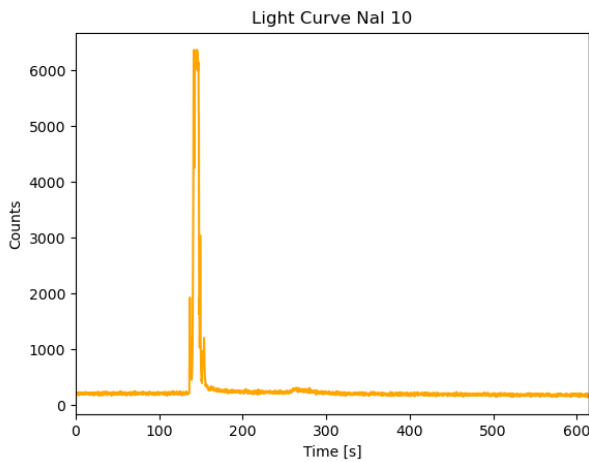


**Figure 29:** Light Curve detected by NaI10' detector.

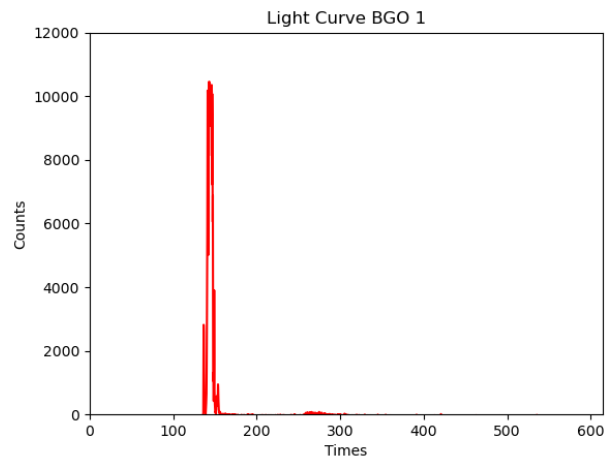


**Figure 32:** Light Curve detected by BGO1 detector.

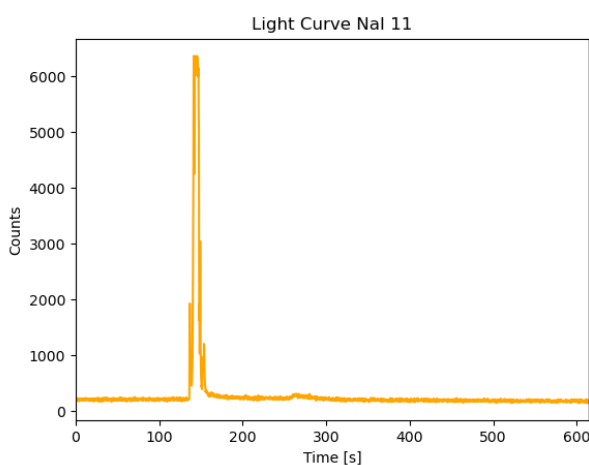


**Figure 30:** Light Curve detected by NaI11 detector.

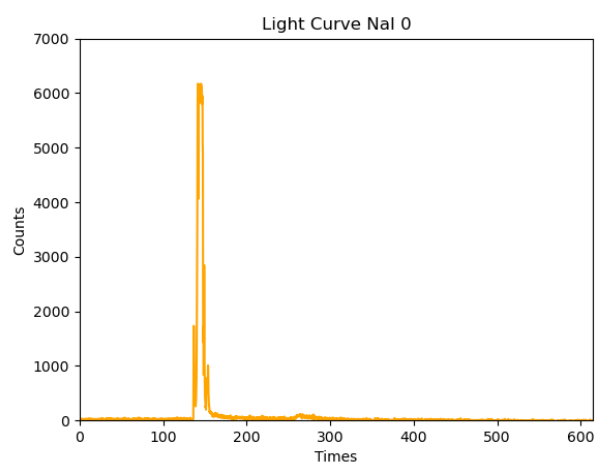


**Figure 33:** Light Curve detected by NaI0 detector.

## 8.2 Light Curve after subtracting Background

Fig. 31-44 show the background subtracted light curves.

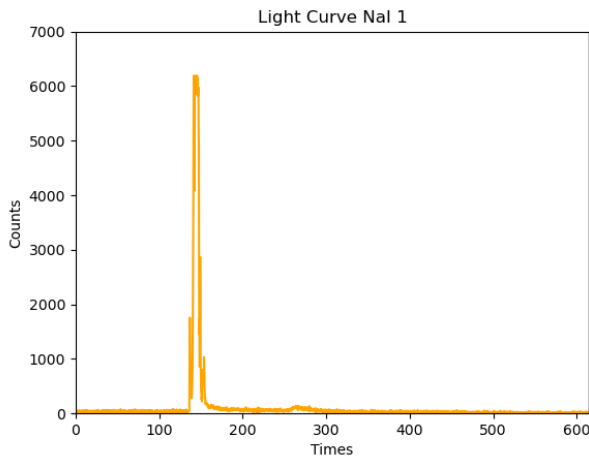


**Figure 34:** Light Curve detected by NaI1 detector.

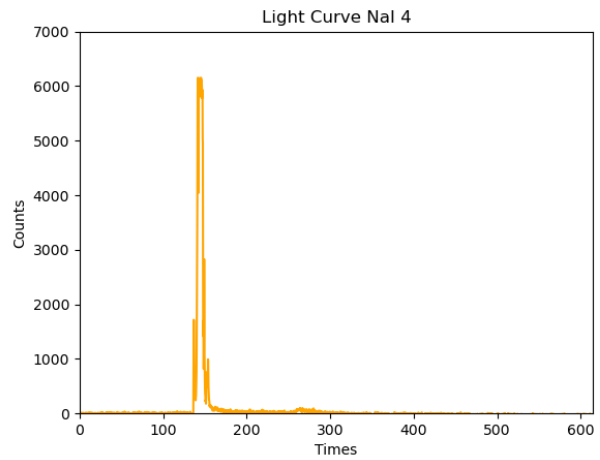


**Figure 37:** Light Curve detected by NaI4 detector.

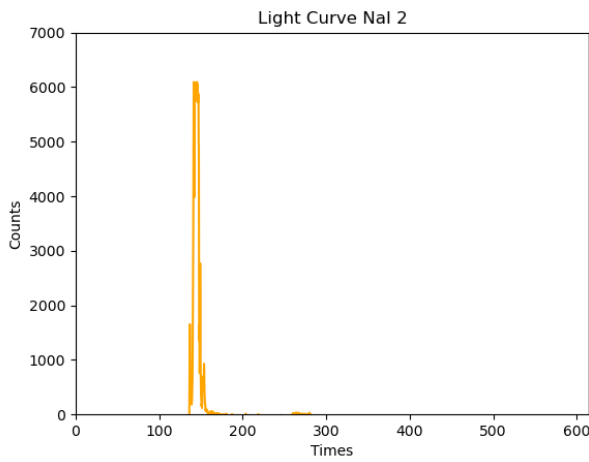


**Figure 35:** Light Curve detected by NaI2 detector.

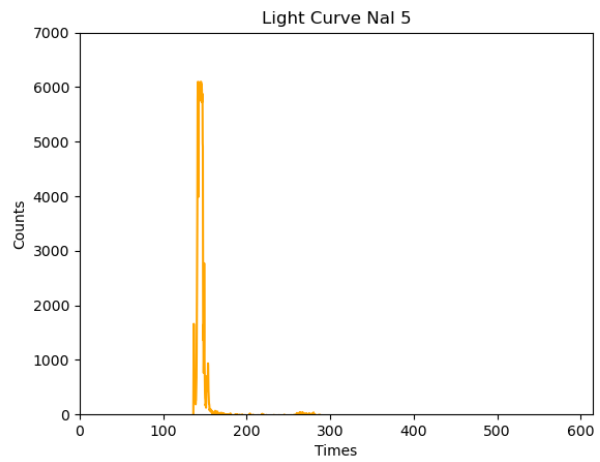


**Figure 38:** Light Curve detected by NaI5 detector.

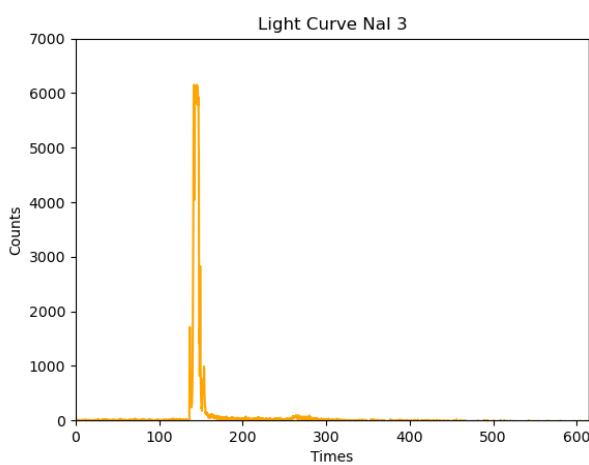


**Figure 36:** Light Curve detected by NaI3 detector.

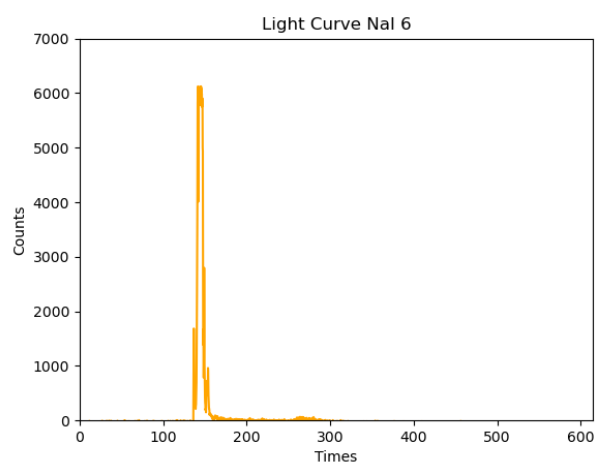


**Figure 39:** Light Curve detected by NaI6 detector.

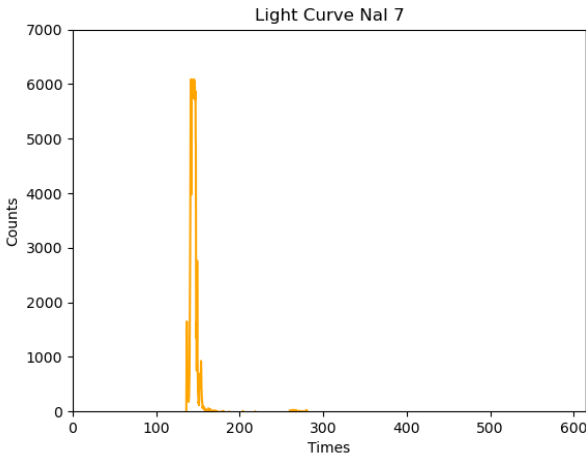


**Figure 40:** Light Curve detected by NaI7 detector.

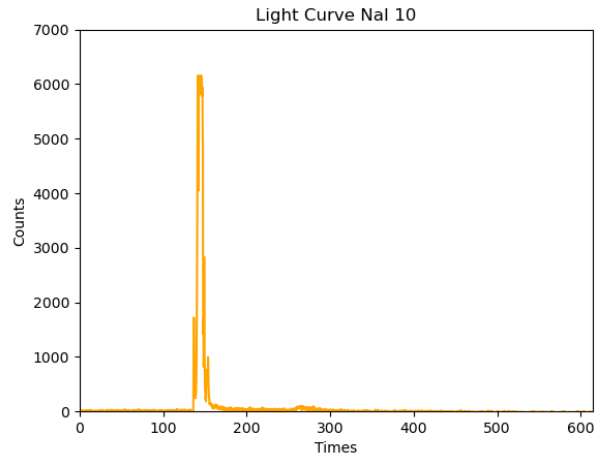


**Figure 43:** Light Curve detected by NaI10 detector.

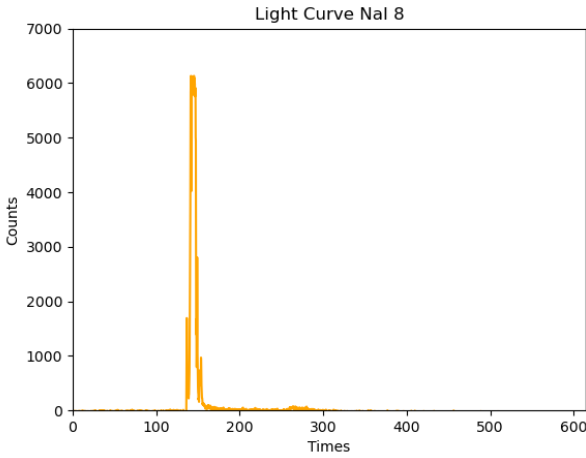


**Figure 41:** Light Curve detected by NaI8 detector.

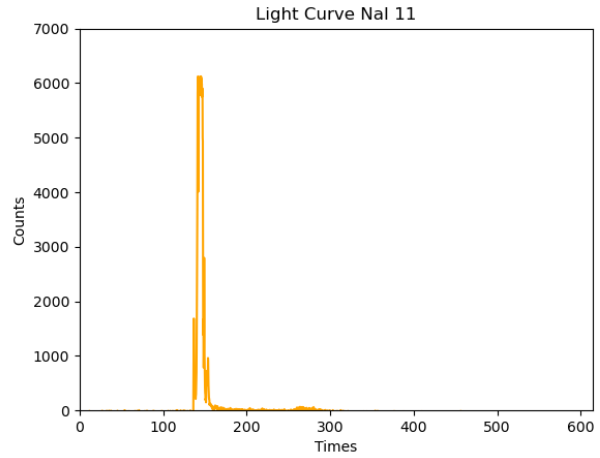


**Figure 44:** Light Curve detected by NaI11 detector.

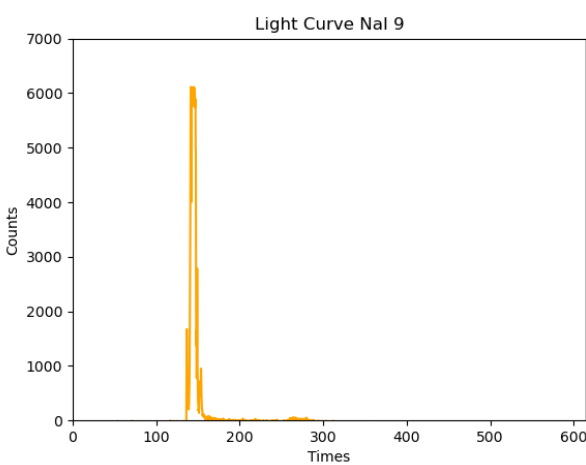


**Figure 42:** Light Curve detected by NaI9 detector.

### 8.3 Light Curve thanks to GBM Data Tools employed in the Spectral Analysis

Fig. 45-47 show the light curves computed and plotted with GBM Data Tools for the three detectors used.

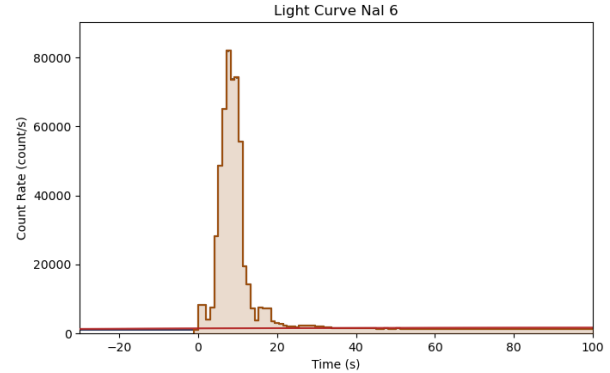


**Figure 45:** Light Curve detected by NaI6 detector analysed by GBM Data Tools

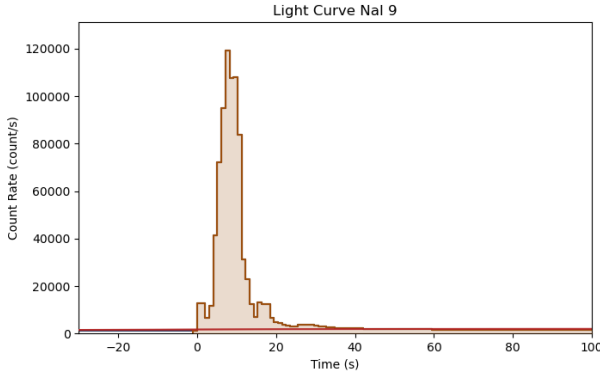


**Figure 46:** Light Curve detected by NaI9 detector analysed by GBM Data Tools

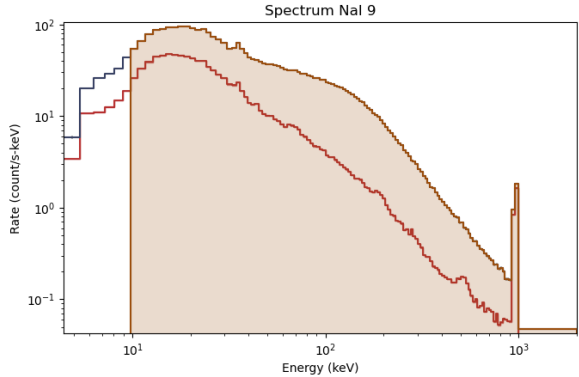


**Figure 49:** Energy-spectrum by NaI9 detector analysed by GBM Data Tools

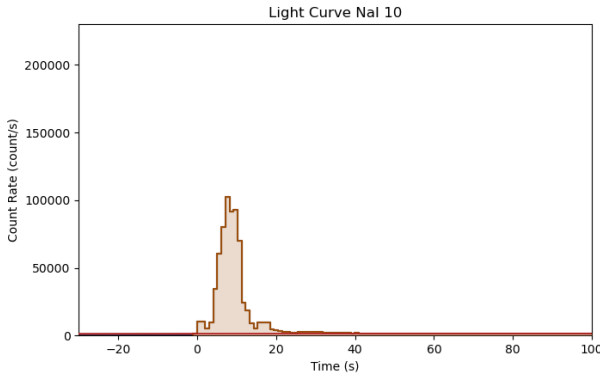


**Figure 47:** Light Curve detected by NaI10 detector analysed by GBM Data Tools

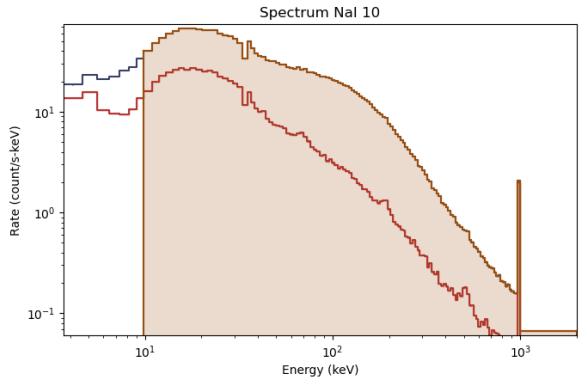


**Figure 50:** Energy-spectrum by NaI10 detector analysed by GBM Data Tools

#### 8.4 Spectra thanks to GBM Data Tools employed in the Spectral Analysis

Fig. 48–50 show the energy-spectra computed and plotted with GBM Data Tools for the three detectors used.

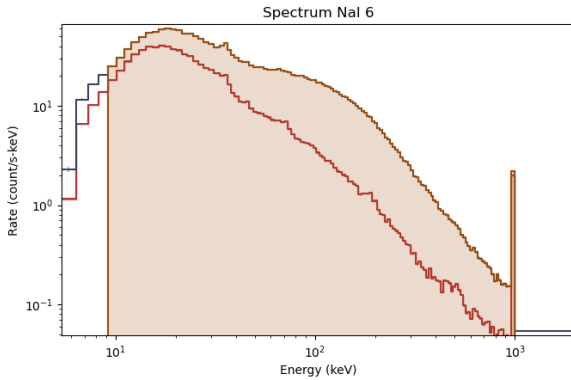


**Figure 48:** Energy-spectrum by NaI6 detector analysed by GBM Data Tools

#### References

- [1] Lorenzo Amati. “The  $E_{p,i}$  -  $E_{\text{iso}}$  correlation in GRBs: updated observational status, re-analysis and main implications”. In: *Monthly Notices of the Royal Astronomical Society* (2006). Submitted on 24 Jan 2006, last revised 20 Jul 2006. arXiv: [astro-ph/0601553](https://arxiv.org/abs/astro-ph/0601553) [astro-ph]. URL: <https://arxiv.org/abs/astro-ph/0601553>.
- [2] Fermi Science Support Center. *Overview of the Fermi Gamma-ray Burst Monitor (GBM)*. Last updated January 14, 2020. 2020. URL: [https://fermi.gsfc.nasa.gov/ssc/data/analysis/documentation/Cicerone/Cicerone\\_Introduction/GBM\\_overview.html](https://fermi.gsfc.nasa.gov/ssc/data/analysis/documentation/Cicerone/Cicerone_Introduction/GBM_overview.html).
- [3] Adam Goldstein, William H. Cleveland, and Daniel Kocevski. *Fermi GBM Data Tools: v1.1.1*. 2022. URL: <https://fermi.gsfc.nasa.gov/ssc/data/analysis/gbm>.
- [4] HEASARC. *Fermi GBM Burst Catalog*. Accessed: 2025-06-26. 2025. URL: <https://heasarc.gsfc.nasa.gov/db-perl/W3Browse/w3table.pl?tablehead=name%3Dfermigbrst&Action=More+Options>.
- [5] A. von Kienlin and the Fermi GBM Team. *GRB 130427A: Fermi GBM observation*. GCN Circular #14473. Posted 2013-04-27 at 20:27:19 UTC. Apr. 2013. URL: <https://gcn.nasa.gov/circulars/14473>.

- [6] A. von Kienlin et al. “The Fourth Fermi-GBM Gamma-Ray Burst Catalog: A Decade of Data”. In: *arXiv preprint arXiv:2002.11460* (2020). arXiv: 2002.11460 [astro-ph.HE]. URL: <https://arxiv.org/abs/2002.11460>.
- [7] A. von Kienlin et al. “The Fourth Fermi-GBM Gamma-Ray Burst Catalog: A Decade of Data”. In: *The Astrophysical Journal* 893.1 (Apr. 2020). 14 pages, p. 46. DOI: [10.3847/1538-4357/ab80f2](https://doi.org/10.3847/1538-4357/ab80f2).
- [8] A. Maselli et al. “GRB 130427A: A nearby ordinary monster”. In: *Science* 343.6166 (2014), pp. 48–51. DOI: [10.1126/science.1242279](https://doi.org/10.1126/science.1242279). URL: <https://www.science.org/doi/10.1126/science.1243697>.
- [9] Sergio Ortolani. *Dispense del corso di Astronomia, Università di Padova*.